Biogeosciences, 12, 5229–5245, 2015
www.biogeosciences.net/12/5229/2015/
doi:10.5194/bg-12-5229-2015

Biogeosciences Open Access

Reconstruction of super-resolution ocean pCO_2 and air–sea fluxes of CO_2 from satellite imagery in the southeastern Atlantic

I. Hernández-Carrasco[1], J. Sudre[1], V. Garçon[1], H. Yahia[2], C. Garbe[3], A. Paulmier[1], B. Dewitte[1], S. Illig[1], I. Dadou[1], M. González-Dávila[4], and J. M. Santana-Casiano[4]

[1]LEGOS, Laboratoire d'Études en Géophysique et Océanographie Spatiales (CNES-CNRS-IRD-UPS), 31401 Toulouse, France
[2]INRIA, Institut National de Recherche en Informatique et en Automatique, Bordeaux, France
[3]IWR, Interdisciplinary Center for Scientific Computing, University of Heidelberg, Heidelberg, Germany
[4]Instituto de Oceanografía y Cambio Global, Universidad de Las Palmas de Gran Canaria, 35017, Las Palmas de Gran Canaria, Spain

Correspondence to: I. Hernández-Carrasco (ismael.hernandez@legos.obs-mip.fr)

Received: 26 October 2014 – Published in Biogeosciences Discuss.: 21 January 2015
Revised: 29 July 2015 – Accepted: 16 August 2015 – Published: 11 September 2015

Abstract. An accurate quantification of the role of the ocean as source/sink of greenhouse gases (GHGs) requires to access the high-resolution of the GHG air–sea flux at the interface. In this paper we present a novel method to reconstruct maps of surface ocean partial pressure of CO_2 (pCO_2) and air–sea CO_2 fluxes at super resolution (4 km, i.e., 1/32° at these latitudes) using sea surface temperature (SST) and ocean color (OC) data at this resolution, and CarbonTracker CO_2 fluxes data at low resolution (110 km). Inference of super-resolution pCO_2 and air–sea CO_2 fluxes is performed using novel nonlinear signal processing methodologies that prove efficient in the context of oceanography. The theoretical background comes from the microcanonical multifractal formalism which unlocks the geometrical determination of cascading properties of physical intensive variables. As a consequence, a multi-resolution analysis performed on the signal of the so-called singularity exponents allows for the correct and near optimal cross-scale inference of GHG fluxes, as the inference suits the geometric realization of the cascade. We apply such a methodology to the study offshore of the Benguela area. The inferred representation of oceanic partial pressure of CO_2 improves and enhances the description provided by CarbonTracker, capturing the small-scale variability. We examine different combinations of ocean color and sea surface temperature products in order to increase the number of valid points and the quality of the inferred pCO_2 field. The methodology is validated using in situ measurements by means of statistical errors. We find that mean absolute and relative errors in the inferred values of pCO_2 with respect to in situ measurements are smaller than for CarbonTracker.

1 Introduction

The ocean can be thought of as a complex system in which a large number of different processes (e.g., physical, chemical, biological, atmosphere–ocean interactions) interact with each other at different spatial and temporal scales (Rind, 1999). These scales extend from millimeters to thousands of kilometers and from seconds to centuries (Dickey, 2003). There is a growing body of evidence that the upper few hundred meters of the oceans are dominated by submesoscale (1–10 km) activity and that this activity is important to understand global ocean properties (Klein and Lapeyre, 2009). Accurately estimating the sources and sinks of greenhouse gases (GHGs) at the air–sea interface requires resolving these small scales (Mahadevan et al., 2004). However, the scarcity of oceanographic cruises and the lack of available satellite products for GHG concentrations at high resolution prevent us from obtaining a global assessment of their spatial variability at small scales. For example, from the in situ ocean measurements the uncertainty of the net global ocean–atmosphere CO_2 fluxes is between 20 and 30 % (IOCCP, 2007), and

could be higher in the oxygen minimum zones (OMZ) of the eastern boundary upwelling systems (EBUSs) due to the extreme regional variability in these areas (Paulmier et al., 2008; Franco et al., 2014). Indeed, this supports the design of proper methodologies to infer fluxes at high resolution from presently available satellite image data in order to improve current estimates of gas exchanges between the ocean and the atmosphere.

The most commonly used methods to estimate air–sea CO_2 fluxes are based either on statistical methods, inverse modeling with atmospheric transport models or global coupled physical–biogeochemical models. Among others, Takahashi et al. (2002, 2009) interpolate sea surface pCO_2 measurements with advanced statistical methods to provide climatological monthly maps of air–sea fluxes of CO_2 in the global surface waters at a spatial resolution of $4^\circ \times 5^\circ$. Global maps at the same spatial resolution but at higher temporal resolution (daily) have been estimated by Rödenbeck et al. (2014) by fitting the mixed-layer carbon budget equation to ocean pCO_2 observations. An international effort to compile global surface CO_2 fugacity (fCO_2) measurements has recently been performed and reported in Pfeil et al. (2013); Bakker et al. (2014), and interpolated by Sabine et al. (2013), generating a monthly gridded product with fCO_2 values in a $1^\circ \times 1^\circ$ grid cell. Other statistical approaches based on the neural-network statistical method have been shown to be useful to estimate climatological and monthly $1^\circ \times 1^\circ$ maps of pCO_2 (Landschützer et al. (2014) and Telszewski et al. (2009), respectively). Gruber et al. (2009) used inverse modeling of sources and sinks from the network of atmospheric CO_2 concentrations jointly with transport models. The third type of method is based on direct computations of the air–sea CO_2 fluxes in coupled physical–biogeochemical models incorporating the biogeochemical processes of the carbon dioxide system. In this method, simulated surface ocean pCO_2 can be constrained with available ship observations as shown by Valsala and Maksyutov (2010).

Another new avenue for inferring air–sea GHG fluxes is through inverse modeling applied to vertical column densities (VCDs) extracted from satellite spectrometers, i.e., Greenhouse gases Observing SATellite (GOSAT) and SCanning Imaging Absorption SpectroMeter for Atmospheric CHartographY (SCIAMACHY), at low spatial resolution (Garbe and Vihharev, 2012). A global estimation of CO_2 fluxes in the ocean has been derived at $1^\circ \times 1^\circ$ spatial resolution from global atmosphere observations used in a data assimilation system for CO_2 called CarbonTracker (Peters et al., 2007). In all these data sets the rather coarse spatial resolution leads to uncertainties in the actual estimate of the sources and sinks of CO_2, calling for an improvement of the resolution of CO_2 flux estimates.

In this regard, the last few years have seen the appearance of interesting new developments on multiscale processing techniques for complex signals coming from Earth observations (Yahia et al., 2010). These methods make use of phenomenological descriptions of fully developed turbulence (FDT) in nonlinear physics, motivated by the values taken on by the Reynolds number in ocean dynamics. As predicted from the theory and also observed in the ocean, in a turbulent flow the coherent vortices (eddies) interact with each other stretching and folding the flow, generating smaller eddies or small-scale filaments and transition fronts characterized by strong tracer gradients (Frisch, 1995). This results in a cascade of energy from large to smaller scales. Therefore the inherent cascade of tracer variance under the turbulent flow dominates the variability of the geometrical distribution of tracers such as temperature or dissolved inorganic carbon, as shown by Abraham et al. (2000), Abraham and Bowen (2002) and Turiel et al. (2005). Geometrical organization of the flow linked to the energy cascade allows for the study of its properties from the geometrical properties of any tracer for which the advection is the dominant process. The relationships between the cascade and the multifractal organization of FDT has been set up either with canonical (Arneodo et al., 1995; Frisch, 1995) or microcanonical (Turiel et al., 2005; Bouchet and Venaille, 2012) descriptions. Within the microcanonical framework (MMF) the singularity exponents unlock the geometrical realization of the multifractal hierarchy. Setting up a multi-resolution analysis on the singularity exponents computed in the microcanonical framework allows near optimal cross-scale inference of physical variables (Sudre et al., 2015).

These advances open a wide field of theoretical and experimental research and their use in the analysis of complex data coming from satellite imagery has been proven innovative and efficient, showing a particular ability to perform fusion of satellite data acquired at different spatial resolutions (Pottier et al., 2008) and to reconstruct from satellite data current maps at submesoscale resolution (Sudre et al., 2015). In this paper we apply these novel techniques emerging from nonlinear physics and nonlinear signal processing for inferring submesoscale resolution maps of the air–sea CO_2 fluxes and associated sinks and sources from available remotely sensed data. We use this methodology to derive cross-scale inference according to the effective cascade description of an intensive variable, through a fusion process between appropriate physical variables which account for the flux exchanges between the ocean and the atmosphere. This approach is not only very novel in signal processing, but also connects the statistical descriptions of acquired data with their physical content. This makes the approach useful to reconstruct all GHGs.

Unlike the Lagrangian approach to reconstruct tracer maps at high resolution (Berti and Lapeyre, 2014), our methodology works in the Eulerian framework and we do not need to know the trajectories of oceanic tracer particles, but only high-resolution instantaneous maps of tracers which can be directly obtained from remote sensing.

The eastern boundary upwelling systems (EBUSs) and oxygen minimum zones (OMZs) are likely to contribute sig-

nificantly to the gas exchange between the ocean and the atmosphere (Hales et al., 2005; Waldron et al., 2009; Paulmier et al., 2011). The Benguela upwelling system, the region of interest in this study, is one of the highest productivity areas in the world ocean and may contribute significantly to the global air–sea CO_2 flux. Some studies using data from in situ samples have found the region of Benguela to be an annual sink of CO_2 with uptakes of -1.70 (in 1995 and 1996) and $-2.02\,\mathrm{Mt\,C\,yr^{-1}}$ in 2005 (Santana-Casiano et al., 2009; Monteiro, 2010), with a strong variability between 2005 and 2006 from -1.17 to $-3.24\,\mathrm{mol\,C\,m^{-2}}$ per year, respectively (González-Dávila et al., 2009).

This paper is organized as follows: Sect. 2 describes the data sets used as input in our algorithm. Section 3 describes the methodology used through the study. Statistical description of the input data sets is presented in Sect. 4. Results of the inference method are given in Sect. 5 by providing outputs of our algorithm, then evaluating the various satellite products and assessing the performance of the method using in situ measurements.

2 Data

The input data combines air–sea CO_2 fluxes at low resolution and satellite ocean data at high resolution. To validate the method we use in situ measurements of oceanic pCO_2.

2.1 Input data: air–sea CO_2 fluxes at low resolution

It is known that the evolution of a concentration, c, in the atmosphere is given by the advection–reaction–diffusion equation:

$$\frac{\partial c}{\partial t} = -u\nabla c + \frac{1}{\rho}\nabla(\rho T_\mathrm{d}\nabla c) + \frac{1}{\rho}g + F, \quad (1)$$

with the wind field u, the density of the air ρ, the turbulent diffusivity tensor T_d, the chemical reaction rate g and the net flux at the air–sea interface F (Garbe et al., 2007, 2014). Using optimal control and inverse problem modeling, a map of F can be derived using Earth observation data (Garbe and Vihharev, 2012). It would be ideal if we could use data of atmospheric CO_2 concentrations from space measured by satellite sensors such as SCIAMACHY (SCanning Imaging Absorption SpectroMeter for Atmospheric CHartographY) aboard ENVISAT (Environmental Satellite), in orbit since 2002, and GOSAT (Greenhouse gases Observing SATellite), in orbit since January 2009, to derive the air–sea flux. However SCIAMACHY and GOSAT sampling is not dense enough, with very suboptimal sampling of the Benguela upwelling system. This led us to use data of CO_2 fluxes from CarbonTracker (http://www.esrl.noaa.gov/gmd/ccgg/carbontracker/) at spatial resolution of $1^\circ \times 1^\circ$ ($\sim 100\,\mathrm{km} \times \sim 100\,\mathrm{km}$) (Peters et al., 2007). CarbonTracker system assimilates and integrates a diversity of atmospheric CO_2 data into a computation of surface CO_2 fluxes, using a state-of-the-art atmospheric transport model and an ensemble Kalman filter.

We obtain the partial pressure of ocean CO_2 by using the equation of the net flux in the air–sea interface:

$$F = \alpha K(p^{\mathrm{air}}_{\mathrm{CO_2}} - p^{\mathrm{ocean}}_{\mathrm{CO_2}}), \quad (2)$$

where α is the gas solubility, which depends on sea surface temperature (SST) and sea surface salinity (SSS), and K, the gas transfer velocity, is a function of wind, salinity, temperature, and sea state, which can be obtained from satellite data. To estimate the gas transfer velocity we use well-accepted relationships for the transfer velocity in air–sea gas exchange from wind speed, the parameterization developed by Sweeney et al. (2007). The CO_2 gas solubility is derived according to Weiss (1974). Input data for SST are derived from OSTIA (Operational SST and Sea Ice Analysis system) product, SSS are derived from LEGOS (Laboratoire d'Etudes en Géophysique et Océanographie Spatiales) product compiled by Delcroix et al. (2011) and winds from Cross-Calibrated Multi-Platform Ocean surface winds from JPL (Jet Propulsion Laboratory) PO.DAAC (Physical Oceanography Distributed Active Archive Center, http://podaac.jpl.nasa.gov/). We assume $p^{\mathrm{air}}_{\mathrm{CO_2}}$ to be constant in the domain of study, and it is derived from the Globalview-CO2 product of the Cooperative Atmospheric Data Integration Project coordinated by Carbon Cycle Greenhouse Gases Group (GLOBALVIEW, 2013) (www.esrl.noaa.gov/gmd/ccgg/globalview/). We use values taken at the closest sea-level station to the Benguela, located at Ascension Island (7.97° S and 14.40° W) as our reference atmospheric CO_2. The partial pressure of CO_2 is determined from its mole fraction ($x\mathrm{CO_2}$), using the following equation (Dickson et al., 2007): $p\mathrm{CO_2} = x\mathrm{CO_2} \times p$, where p is the total pressure of the mixture. We assume this pressure to be close to 1 atm for the conversion following ORNL/CDIAC 105 report (program developed for CO_2 systems calculation).

The raw data of CarbonTracker fluxes of CO_2 in the area of interest are strongly binned and exhibit strong gradients across those bins. This turns out to be suboptimal for our super-resolution approach. Garbe and Vihharev (2012) developed an optimal control approach to invert interfacial fluxes using a simplified inverse problem of atmospheric transport. The inverse problem is solved using the Galerkin finite element method and the dual weighted residual (DWR) method for goal-oriented mesh optimization. An adaptation of this approach has been applied to the CarbonTracker data set. However, the estimations are expensive and computing results for all the time frames of interest was infeasible. Therefore, an anisotropic diffusion-based approach has been applied to the raw fluxes of the CarbonTracker data set. The diffusion is steered by the direction of the low-altitude wind field. The results thus retain the structure of the CarbonTracker fluxes very well while suppressing artifacts. Examples of this process are shown in Fig. 1. Results are compa-

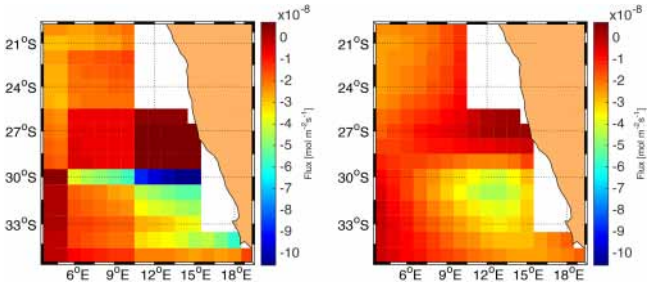

Figure 1. Estimated fluxes from CarbonTracker data. Shown are the results on the Benguela upwelling system on 23 March 2006. Left are the CarbonTracker fluxes, right are our results.

rable to the physically more accurate approach of Garbe and Vihharev (2012).

2.2 Input data: satellite ocean data at high resolution

Oceanic pCO_2 is a complex signal depending, at any spatial resolution, on sea surface temperature, salinity, chlorophyll concentration, dissolved inorganic carbon, alkalinity and nutrient concentrations. Both the biological pump, with chlorophyll *a* as a proxy, and the physical pump, driven by the temperature and salinity (e.g., solubility, water mass), govern the evolution of pCO_2 in the surface ocean.

We use here the high-resolution satellite ocean data for chlorophyll *a*, as a proxy for the biological carbon pump and for SST, as a proxy for the thermodynamical pump, (see Sect. 3.2 for more details on the connection of these oceanic variables).

2.2.1 Chlorophyll *a* (Chl *a*) from ocean color (OC)

In this study we use Chl *a* concentrations from two different ocean color products: MERIS and GLOBCOLOUR. MERIS (MEdium Resolution Imaging Spectrometer Instrument) is on board the ENVISAT satellite and provides daily maps of ocean color at $1/24°$ (~ 4 km). Ocean color from GLOBCOLOUR product is obtained by merging data provided by MODIS (MODerate Resolution Imaging Spectroradiometer), MERIS and SeaWiFS (Sea-viewing Wide Field-of-view Sensor) instruments. The Chl *a* concentration is provided daily and at the spatial resolution equal to $1/24°$ (~ 4 km). Ocean color data have been regridded at $1/32°$ by linear interpolation. GLOBCOLOUR products are generated using different merging methods (see the GLOBCOLOUR Product User Guide document in http://www.globcolour.info/CDR_Docs/GlobCOLOUR_PUG.pdf):

- *Averaging from single-instrument Chl a concentration.* In this case CHL1 daily level 3 (L3) products are generated for each instrument using the corresponding L2 data. At the beginning of the averaging process, an intercalibration correction is applied to the MODIS and SeaWiFS CHL1 daily L3 products in order to get compatible concentrations with respect to the MERIS sensor. The merged CHL1 concentration is then computed as the average of the MERIS, MODIS and SeaWiFS quantities, both as an *arithmetic mean* or a *weighted average value (AVW)*. In the AVW method, values of CHL1 are weighted by the relative error for each sensor on the results of the simple averaging.

- *Garver–Siegel–Maritorena model (GSM).* In this method single-instrument daily L3 fully normalized water leaving radiances (individually computed for each band) and their associated error bars are used by the GSM model. These radiances are not intercalibrated before incorporation in the model (see Maritorena and Siegel, 2005, for more details).

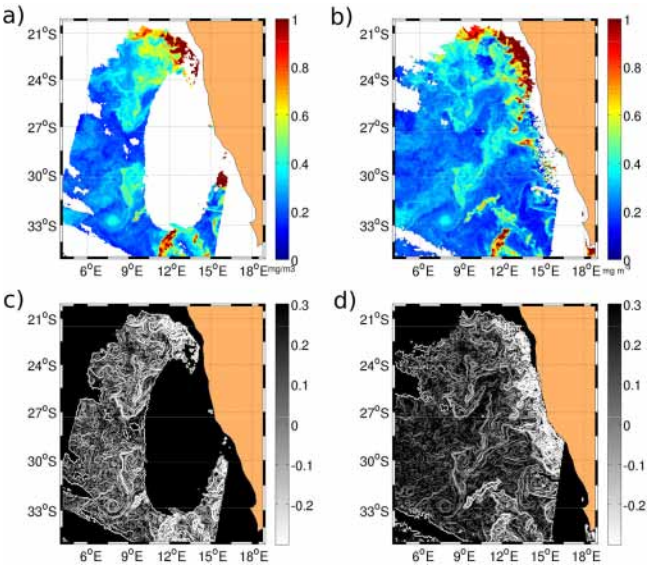

Figure 2. Snapshot of Chl *a* fields corresponding to 21 September 2006, regridded at $1/32°$ of spatial resolution from MERIS **(a)** and GSM GLOBCOLOUR **(b)**. **(c)** and **(d)** are the spatial distribution of singularity exponents of the Chl *a* plotted in **(a)** and **(b)**, respectively.

Snapshots of both Chl *a* fields derived from MERIS and GSM GLOBCOLOUR corresponding to 21 September 2006 are displayed in Fig. 2a and b, respectively. This example shows the clear difference in the remote sensing coverage between the two products. The merged GLOBCOLOUR product yields a more covered Chl *a* field than the one obtained from MERIS. The merging algorithm in the GLOBCOLOUR product tends to decrease the missing points induced by clouds for each individual instrument.

2.2.2 Sea surface temperature (SST)

We use SST derived from OSTIA and MODIS products. OSTIA (Operational SST and Sea Ice Analysis system) is a new analysis of SST that uses satellite data provided by

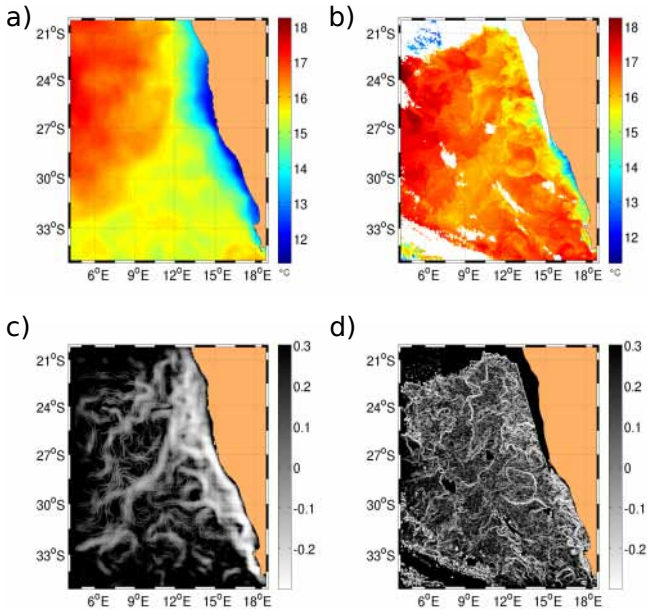

Figure 3. Snapshot of SST fields corresponding to 21 September 2006 regridded at $1/32°$ of spatial resolution from OSTIA **(a)** and MODIS **(b)**. **(c)** and **(d)** are the spatial distribution of singularity exponents of the SST plotted in **(a)** and **(b)**, respectively.

the GHRSST (Group for High Resolution SST) project, together with in situ observations, to determine the SST with a global coverage and without gaps in data. The data sets are produced daily and at spatial resolution of $1/20°$ (~ 6 km) performing a multi-scale optimal interpolation using correlation length scales from 10 to 100 km (more details in Donlon et al., 2012). The other SST product used in this study is derived from MODIS (MODerate Resolution Imaging Spectroradiometer) sensors carried on board the Aqua satellite since December 2002. This SST product is derived from the MODIS mid-infrared (IR) and thermal IR channels and is available in various spatial and temporal resolutions. We use Level-3 daily maps of SST at the spatial resolution of $1/24°$ (~ 4 km) (Savtchenko et al., 2004). In Fig. 3a and b, we show one snapshot of SST from OSTIA and MODIS, respectively corresponding to the same day on 21 September 2006. In the case of OSTIA products, the SST field is fully covered with points while for MODIS products there are gaps due to cloudiness. On other hand, MODIS product offers a more detailed visualization of the small structures. All SST data have been regridded at $1/32°$ by bilinear interpolation.

2.3 Validation data: in situ measurements

Among the available data in SOCAT version 2 (Bakker et al., 2014) (Surface Ocean CO_2 Atlas, http://www.socat.info) over the 2000–2010 period in our region of interest, we find the following cruises with pCO_2 measurements:

- 2000, one cruise: ANT-18-1
- 2004, one cruise: 0404SFC-PRT
- 2005, five cruises: QUIMA2005-0804, QUIMA2005-0821, QUIMA2005-0922, QUIMA2005-1202, QUIMA2005-1220
- 2006, nine cruises: GALATHEA, QUIMA2006-0326, QUIMA2006-0426, QUIMA2006-0514, QUIMA2006-0803, QUIMA2006-0821, QUIMA2006-0921, QUIMA2006-1013, QUIMA2006-1124
- 2008, seven VOS cruises: QUIMA2008-1, QUIMA2008-2, QUIMA2008-3, QUIMA2008-4, QUIMA2008-5, QUIMA2008-6, QUIMA2008-7
- 2010, one cruise: ANT27-1

The small number of cruises found in 1 decade (24 cruises) shows that the scarcity of cruises in the Benguela region is a fact. This indeed demonstrates the crucial need of developing a robust method to infer high-resolution pCO_2 from space. Moreover for some of these cruises, for instance, the track of GALATHEA cruise is too close to the coast and is out of the original CarbonTracker domain. Due to this restriction we only document the offshore conditions of this upwelling system. Owing to the relatively large number of cruises during 2005, 2006 and 2008 (a total of 20 cruises, representing 83 % of all available cruise data from 2000 through 2010), in this validation, we focus the analysis on the set of QUIMA-cruises during 2005 (QUIMA2005), 2006 (QUIMA2006) and 2008 (QUIMA2008) and we present the global analysis using all available cruises during these 3 years. Santana-Casiano et al. (2009) analyzed this data to study the sea surface pCO_2, fCO_2 and CO_2 air–sea fluxes in the offshore Benguela upwelling system between 2005 and 2006 (for each month from July 2005 up to November 2006) and González-Dávila et al. (2009) extended the study including cruises data from 2007 to 2008. The QUIMA line crosses the region between 5 and 35° S, with all the cruises following the same track.

3 Method

The idea behind the methodology hinges on the fundamental discovery of a simple functional dependency between the transitions – those being measured by the dimensionless values of the singularity exponents computed within the framework of the microcanonical multifractal formalism – of the respective physical variables under study: SST, ocean color and oceanic partial pressure (pCO_2). With that functional dependency being adequately fitted into a linear regression model, it becomes possible to compute, at any given time, a precise evaluation of pCO_2 singularity exponents using SST, ocean color and low resolution acquired pCO_2. Once these singularity exponents are computed, they generate a multi-resolution analysis from which low-resolution pCO_2 can

be cross-scale-inferred to generate a high-resolution pCO_2 product. In this study we choose SST and Chl a, and not other variables such as sea surface height, because we focus on the use of physical variables which are correlated spatially and temporally to pCO_2 and that can be obtained from satellite at high resolution.

3.1 Singularity exponents and the multifractal hierarchy of turbulence

In the ocean, the turbulence causes the formation of unsteady eddies on many scales which interact with each other (Frisch, 1995). Most of the kinetic energy of the turbulent motion is contained in the large-scale structures. The energy cascades from the large-scale structures to smaller-scale structures by an inertial and essentially inviscid mechanism. This process continues, creating smaller and smaller structures which produces a hierarchy of eddies. Moreover, the ocean is a system displaying scale-invariant behavior, that is, the correlations of variables do not change when we zoom in or we zoom out the system, and can be represented by power laws in particular, with the scaling exponents h.

It can be shown that the scaling exponents are the values taken on by localized singularity exponents, which can be computed at high precision in the acquired data using the microcanonical multifractal formalism. Hence, within that framework, the multifractal hierarchy of turbulence, defined by a continuum of sets (F_h) indexed by scaling exponents (h), is obtained as the level sets of the geometrically localized singularity exponents.

We will not review here the details of the computation of the singularity exponents $h(x)$, leaving the reader to consult references (Turiel et al., 2005, 2008; Pont et al., 2011b; Maji and Yahia, 2014; Sudre et al., 2015) for an effective description of an algorithm able to compute the $h(x)$ at every point x in a signal's domain.

Some examples of the singularity exponents of Chl a and SST images for the different products described in Sect. 2.2 are shown in Figs. 2c, 2d, 3c, 3d, respectively. As compared to the corresponding images of Chl a and SST shown in Figs. 2a, 2b, 3a, 3b, one can see the ability of the singularity exponents to unveil the cascade structures arisen by tracer-gradient variances hidden in satellite images.

3.2 Functional dependencies between the singularity exponents of intensive physical variables

Another important idea implemented in the methodology is the coupling of the physical information contained in SST and OC images with the ocean pCO_2. For instance, it is known that marine primary production is a key process in oceanic carbon cycling, and variations in the concentration of phytoplankton biomass can be related to variations in carbon concentrations. Surface temperature is also related to gas solubility in the ocean, and areas with high temperatures are more suitable for releasing CO_2 to the atmosphere. We have studied the relationship of SST and Chl a variables with pCO_2 using the outputs of a coupled Regional Ocean Modeling System (ROMS) with the BIOgeochemical model of the Eastern Boundary Upwelling System (BIOEBUS) (Gutknecht et al., 2013). The ROMS includes several levels of nesting and composed grids, which makes it an ideal model for the basis of our methodology in working in two spatial resolutions. BIOEBUS has been developed for the Benguela to simulate the first trophic levels of the Benguela ecosystem functioning and also to include a more detailed description of the complete nitrogen cycle, including denitrification and anammox processes as well as the oxygen cycle and the carbonate system. This model coupled to ROMS has been also shown to be skillful in simulating many aspects of the biogeochemical environment in the Peru upwelling system (Montes et al., 2014). When one compares SST and Chl a with pCO_2 one finds undetermined functional dependency. However, when comparing their corresponding singularity exponents one obtains a clear simpler dependency. This is due to the fact that SST, Chl a and pCO_2 are variables of different dimensions while singularity exponents are dimensionless quantities. These results show that there is a good correlation between the turbulent transitions given by the singularity exponents and that singularity exponents are good candidates for a multi-resolution analysis performed on the three signals, SST, Chl a and pCO_2. Furthermore, the log-histograms and singularity spectrum show that singularity exponents of pCO_2 images possess a multifractal character. Therefore, such signals are expected to feature cascading, multiscale and other characteristic properties found in turbulent signals as described in Turiel et al. (2008) and Arneodo et al. (1995). Consequently the use of nonlinear and multiscale signal processing techniques is justified to assess the properties of the pCO_2 signal along the scales.

Therefore, in our methodology, the local connection between different tracer concentrations (SST and Chl a) with pCO_2, is performed in order to obtain a proxy for pCO_2 at high resolution by using the following linear combination of multiple linear regressions:

$$\begin{aligned}\mathsf{S}(pCO_2)(x) = \; & a(x)\mathsf{S}(\mathrm{SST})(x) + b(x)\mathsf{S}(\mathrm{Chl}\ a)(x) + \\ & c(x)\mathsf{S}(pCO_2{}^{\mathrm{LR}})(x) + \mathrm{d}(x), \end{aligned} \tag{3}$$

where $\mathsf{S}(pCO_2)(x)$ refers to the singularity exponent of pCO_2 at x, $\mathsf{S}(\mathrm{SST})(x)$ to singularity exponent of SST at x, $\mathsf{S}(Chl\ \mathrm{a})(x)$ to singularity exponent of Chl a signal at x. In order to propagate the pCO_2 signal itself along the scales in the multi-resolution analysis we introduce $\mathsf{S}(pCO_2{}^{\mathrm{LR}})$ to refer to the singularity exponent from pCO_2 at low resolution interpolated on the high-resolution grid. $a(x)$, $b(x)$ and $c(x)$ are the regression coefficients associated with singularity exponents, and $d(x)$ is the error associated with the multiple-linear regression. These regression coefficients are estimated using simulated data from the ROMS-BIOEBUS model de-

veloped for the Benguela upwelling system and described above.

Once we have introduced these coefficients in the linear combination on satellite data, we obtain a proxy for singularity exponents of pCO_2 at high resolution and we can perform the multi-resolution analysis to infer the information across the scales.

3.3 Cross-scale inference of pCO_2 data

Among the functionals that are most commonly used for analyzing the scaling properties of multifractal systems, wavelets occupy a prominent position. Wavelets projections are integral transforms that separate the relevant details of a signal at different scale levels, and since they are scale-tunable, they are appropriate for analyzing the multiscale behavior of cascade processes and for representing them. However, as shown in Pottier et al. (2008), Yahia et al. (2010) and Pont et al. (2011a), not all multi-resolution analyses are equivalent; the most interesting are those which are optimal for inferring information along scales, in particular, in a context where information is to be propagated along the scales from low resolution to high resolution.

The effective determination of an optimal wavelet for a given category of turbulent signals is, in general, a very difficult open problem. This difficulty can be contoured by considering multi-resolution analysis performed on the signal of the singularity exponents $h(x)$ themselves. Indeed, since the most singular manifold (the set F_h associated with the lowest singularity exponents) is associated with the highest frequencies in a turbulent signal, and since the multifractal hierarchy F_h converges to this set, it is physically evident that the multifractal hierarchy corresponds to a description of the detail spaces of a multi-resolution analysis performed on a turbulent signal. Consequently, designating the approximation and detail spaces computed on the $\mathsf{S}(pCO_2)(x)$ signal as V_j and W_j, respectively, and their corresponding orthogonal projections from space $L^2(R^2)$ as A_j and P_j, the reconstruction formula,

$$A_{j-1}pCO_2 = A_j pCO_2 + P_j h, \tag{4}$$

consists of reconstructing a signal across the scales using the detail spaces of the singularity exponents and hence regenerating a physical variable according to its cascade decomposition. From these ideas, which are described more fully in Sudre et al. (2015), we can deduce the following algorithm for reconstructing a super-resolution pCO_2 signal from available high-resolution SST, Chl a, and low-resolution pCO_2:

(i) After selecting a given area of study, compute the singularity exponents of SST, Chl a and pCO_2 at low and high resolution from ROMS-BIOEBUS output. This is done once and then they can be used for every computation performed over the same area.

(ii) Using Eq. (2) estimate ocean pCO_2 at low resolution: $p^{\text{ocean}}_{CO_2} = p^{\text{air}}_{CO_2} - F/\alpha K$, where:

- F: air–sea surface CO_2 fluxes provided by CarbonTracker product;
- K: gas transfer velocity obtained by the parameterization developed by Sweeney et al, 2007, as a function of the wind.
- α: gas solubility derived according to Weiss (1974);
- $p^{\text{air}}_{CO_2}$: provided by Globalview-CO2 product.

(iii) Obtain the regression coefficients a, b, c and d of Eq. (3) for the singularity exponents obtained in step (ii).

(iv) Calculate the singularity exponents of available satellite SST, Chl a at high resolution and ocean pCO_2 at low resolution (step i).

(v) Use coefficients obtained in step (iii) and apply Eq. (3) to the singularity exponents from satellite data (step iv) to estimate a proxy of singularity exponents of high-resolution ocean pCO_2, $\mathsf{S}(pCO_2)$.

(vi) Using Eq. (4), reconstruct pCO_2 at high resolution from the multi-resolution analysis computed on signal $\mathsf{S}(pCO_2)$ and cross-scale inference on pCO_2 at low resolution.

(vii) Use Eq. (2) to calculate air–sea CO_2 fluxes from the inferred pCO_2 obtained in step (vi).

The methodology has been successfully applied to dual ROMS simulation data at two resolutions, obtaining a mean absolute error of pCO_2 reconstructed values with respect to ROMS simulated high-resolution pCO_2 equal to 3.2 µatm (0.89 % of relative error) (V. Garçon, personal communication, 2014).

4 Preliminary analysis of sea surface temperature (SST) and chlorophyll *a* images

Since the key element for the application of our inferring algorithm relies on the ability to obtain the singularity exponents and their quality, the success of our methodology applied to satellite data depends on the quality and the properties of the input data. In order to assess such properties, we perform a statistical analysis of the different data sets. First, we analyze the Chl a and SST probability distribution functions (PDFs). In Fig. 4a we present the PDFs for Chl a from MERIS, GLOBCOLOUR-GSM and GLOBCOLOUR-AVW; the required histograms are built using daily Chl a values over 2006 and 2008 at each point of the spatial grid in the area of Benguela. Each one of these PDFs is broad and asymmetric, with a small mode (i.e., the value of Chl a at which the probability reaches its maximum) between 0.1

Table 1. Values of the standard deviation, skewness and kurtosis for the different products.

PRODUCT	Standard deviation	Skewness	Kurtosis
MERIS	$0.116\,mg\,m^{-3}$	2.6	21.9
GLOBCOLOUR-AVW	$0.122\,mg\,m^{-3}$	4.7	204.6
GLOBCOLOUR-GSM	$0.123\,mg\,m^{-3}$	5.3	215.4
OSTIA	1.97°C	-0.05	1.9
MODIS	2.11°C	-0.17	2.6

Table 2. Values of the standard deviation, skewness and kurtosis of the singularity exponents for the different products.

PRODUCT	Standard deviation	Skewness	Kurtosis
MERIS	$0.32\,mg\,m^{-3}$	0.59	3.1
GLOBCOLOUR-AVW	$0.36\,mg\,m^{-3}$	0.40	3.1
GLOBCOLOUR-GSM	$0.35\,mg\,m^{-3}$	0.63	4.3
OSTIA	0.29°C	1.0	5.1
MODIS	0.32°C	0.5	3.2

and $0.2\,mg\,m^{-3}$ and a heavy tail. The heavy tail (i.e., non-Gaussianity) means that the extreme values can not be neglected. In this case Chl *a* values are mostly low (small mode) but there is a significant number of isolated and dispersed patches with very high Chl *a* values producing intermittency (long tails in the PDF). Intermittency in the context of turbulence is the tendency of the probability distributions of some quantities to develop long tails, i.e., the occurrence of very extreme events.

Further information can be obtained by computing statistical quantities such as standard deviation, skewness and kurtosis. Table 1 shows that standard deviation is rather the same for the three OC products while skewness and kurtosis values differ greatly. The degree of intermittency is measured by the kurtosis, the higher the kurtosis, the higher the intermittency. We found that kurtosis is almost 10 times higher in the GLOBCOLOUR products than in MERIS.

We have repeated the same analysis for SST data sets. The PDFs of the SST values for OSTIA and MODIS products are shown in Fig. 4b. In this case both PDFs possess similar shape, broad with the mode around 18 °C with a much less deviation from Gaussianity as compared to Chl *a* values. This is confirmed with the computation of the statistical moments shown in Table 1. We obtain small values of the standard deviation and kurtosis in both cases, although slightly higher in the case of MODIS. The kurtosis is less than 3, meaning that there is not an important number of atypical values of SST and therefore weak and short tails in the PDFs.

If turbulence is dominated by coherent structures localized in space and time, then PDFs are non-Gaussian, and the kurtosis will be higher than 3. To analyze this feature we turn to the statistical analysis of the singularity exponents, which, as explained before, have the ability to unveil the cascade structures given by the tracer gradients. In Fig. 4c, it can be seen that the PDFs of the singularity exponents of the Chl *a* for the three products are rather similar with almost the same standard deviation and with a slightly higher value of the kurtosis in the GLOBCOLOUR-GSM product, 4.3, than for MERIS, 3.1, and GLOBCOLOUR-AVW, 3.1, (see Table 2). This shows that Chl *a* from GLOBCOLOUR-GSM product contains more extreme values which produce intermittency likely given by the strongest structures. The PDFs of the singularity exponents of the SST for OSTIA is narrower and with a highest peak than for MODIS SST. However, surprisingly the kurtosis is larger for singularity exponents of OSTIA SST, 5.1 than for MODIS SST, 3.2.

Finally, we obtain the singularity spectra from the empirical distributions of singularity exponents shown in Fig. 4c and d. One can see in Fig. 4e that for the two GLOBCOLOUR products the shape of the spectrum is closer to binomial cascade of multiplicative processes than for MERIS. This is discussed in more depth in the next sections.

5 Results

5.1 Inference of super-resolution pCO_2 and air–sea fluxes of CO_2 offshore the Benguela upwelling system

We now apply the methodology to infer ocean pCO_2 maps at super resolution from pCO_2 at low resolution derived from CarbonTracker data (see Sect. 2) in the offshore area of the Benguela region.

Henceforward we use the following notation for the three different sources of pCO_2: we refer to the values of ocean pCO_2 derived from CarbonTracker as pCO_2^{Ctrack}, values of inferred pCO_2 at higher resolution from pCO_2 at low resolution together with computation of the cascade onto SST and chlorophyll *a* concentrations as pCO_2^{infer}, and finally pCO_2^{insitu} refers to the values of the in situ measurements of pCO_2.

For the inference we use the following three combinations of Chl *a* and SST products described in Sect. 2.1: MERIS-OSTIA, GLOBCOLOUR-OSTIA, GLOBCOLOUR-MODIS. We do not include the MERIS-MODIS combination in the analysis due to the fact that the use of such satellite data results in a too drastic reduction of the coverage of the resulting pCO_2^{infer} field, but using merged products offers wider coverage instead. The inferred pCO_2 obtained from two merged products for Chl *a*, GLOBCOLOUR GSM and GLOBCOLOUR AVW is very similar, with a slight improvement when GSM is used. Thus for the sake of clarity, we only show figures for GLOBCOLOUR-GSM and some statistical results making comparisons with AVW. Therefore from now on we use

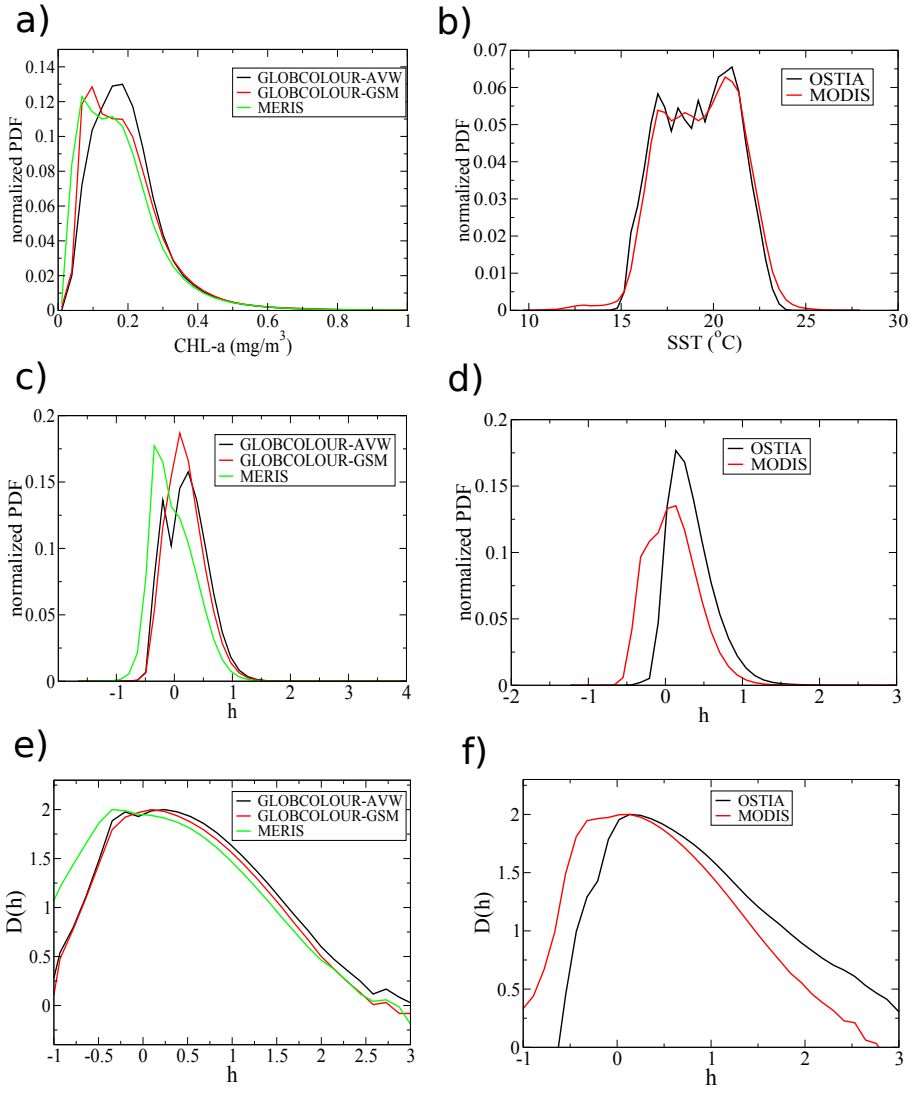

Figure 4. (a) Probability distribution functions (PDF) of Chl *a* values derived from the three products: MERIS, GLOBCOLOUR-AVW and GLOBCOLOUR-GSM. **(b)** PDF of SST values for OSTIA and MODIS products. **(c)** PDFs for the singularity exponents of Chl *a* for the different ocean color products. **(d)** PDFs for the singularity exponents of Chl *a* for the different SST products. **(e)** Singularity spectra corresponding to **(c)**. **(f)** Singularity spectra corresponding to **(d)**.

GLOBCOLOUR to refer to the Chl *a* obtained with the GSM merged method.

Figure 5d shows one example of pCO_2^{infer} field corresponding to 22 March 2006, when we use SST data from OSTIA (Fig. 5a), ocean color from GLOBCOLOUR (Fig. 5b) at high resolution and pCO_2 at low resolution (Fig. 5c) derived from CarbonTracker air–sea flux of CO_2 (Fig. 5e) and using the Eq. (2). The air–sea flux of CO_2 at super resolution (Fig. 5f) is obtained from the pCO_2^{infer} field and a constant value of atmospheric pCO_2 equal to 385.6 µatm. On this day the images of the pCO_2^{infer} and fluxes of CO_2 combine to give good coverage and clear identification of small-scale structures and gradients, as described below. Note that the air–sea CO_2 flux from CarbonTracker presents a large land mask close to the coast and consequently, we study the offshore area of the Benguela upwelling. Comparing the figures one can see that values of pCO_2 and CO_2 flux over the domain (from 4.5° E to coast (taking out the mask of the CarbonTracker domain and from 20.5 to 35° S) vary between 360 and 380 µatm and between -4×10^{-8} and 0.5×10^{-8} mol C m^{-2} s^{-1}, respectively. The resultant flux of CO_2 is positive (towards the atmosphere) in the region 25–28° S and from 7° E eastward to the coast and is negative (into the ocean) south of 30° S and east of 6° E. Thus, we see that in the southern part offshore the Benguela area there is a strong CO_2 sink and the northern part behaves as a weak CO_2 source.

What is new in the reconstructed pCO_2 is, for instance, that the cascade of information across the scales enhances

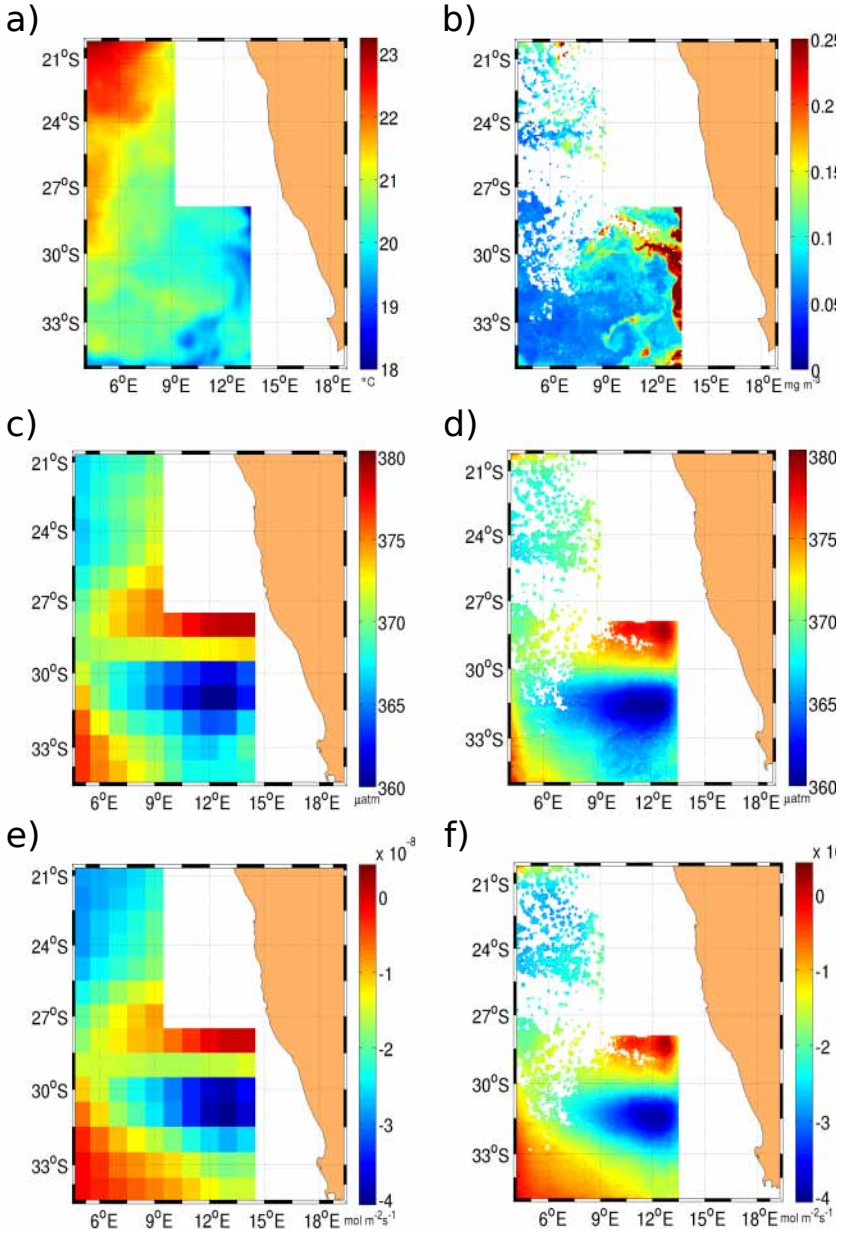

Figure 5. Maps of **(a)** SST from OSTIA at 1/32° of spatial resolution, **(b)** Chl *a* at 1/32° of spatial resolution from GSM GLOBCOLOUR products, **(c)** ocean pCO_2 from CarbonTracker at the spatial resolution of 1°, **(d)** inferred pCO_2 at super resolution (4 km, i.e., 1/32°) derived from OSTIA SST and GLOBCOLOUR-GSM Chl *a* shown in **(a)** and **(b)**, respectively, **(e)** Air–sea CO_2 flux as derived from CarbonTracker and **(f)** Air–sea CO_2 flux computed from super-resolution pCO_2 shown in **(d)** at 1/32°. All images correspond to 22 March 2006. White color corresponds to invalid pixels due to cloudiness and points inside of the CarbonTracker land mask.

gradients in the field of pCO_2. It is striking that the high-resolution map provides the position of the north–south dipole "front" located at 30° S (i.e., -1.5×10^{-8} isoline in green) which could not be inferred accurately from the low-resolution map. The low-resolution map provides an estimate of the location of the "front" that is ∼ 1.5° north of the location inferred from the high-resolution map. Moreover one can see small structures in the pCO_2^{infer} field at 33–35° S, 9–12° E in the pCO_2^{infer} field (Fig. 5d). The small spatial scale variability is captured in the super-resolution pCO_2 field and not in pCO_2^{Ctrack} as shown in the longitudinal profile of the images plotted in Fig. 5 at latitude 33.5° S (see Fig. 6). The same high spatial variability given by the small-scale structures of the SST and OC images can be seen in their corresponding longitudinal profiles displayed in Fig. 6a and b. It is worth noting the change in the shape of the profiles between the pCO_2^{infer} and pCO_2^{Ctrack} and fluxes of CO_2 at large scale,

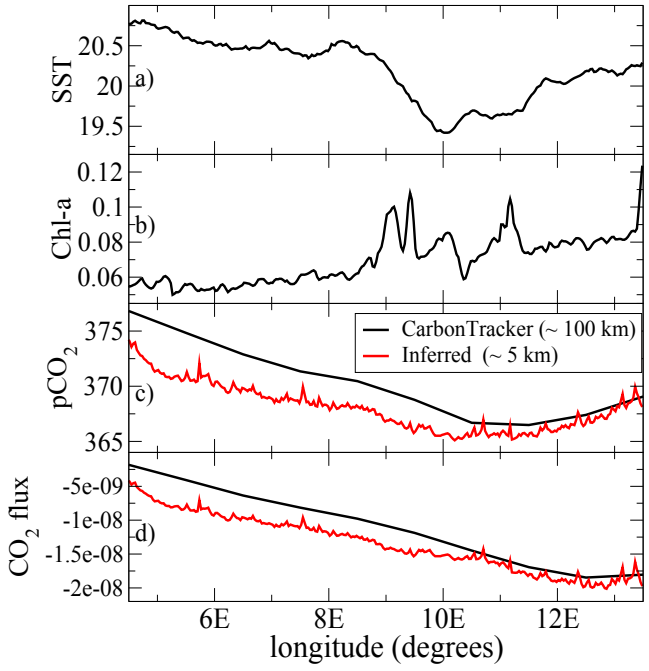

Figure 6. Longitudinal profiles of **(a)** SST from OSTIA products in units of °C, **(b)** Chl *a* from GLOBCOLOUR-GSM ocean in mg m^{-3}, **(c)** pCO_2^{Ctrack} (black line) and pCO_2^{infer} (red line) in µatm, and **(d)** air–sea CO_2 fluxes from CarbonTracker (black line) and inferred air–sea CO_2 fluxes (red line) in mol C m^{-2} s^{-1}. All these longitudinal profiles correspond to the fixed latitude equal to 33.5° S of the plots shown in Fig. 5 for 22 March 2006.

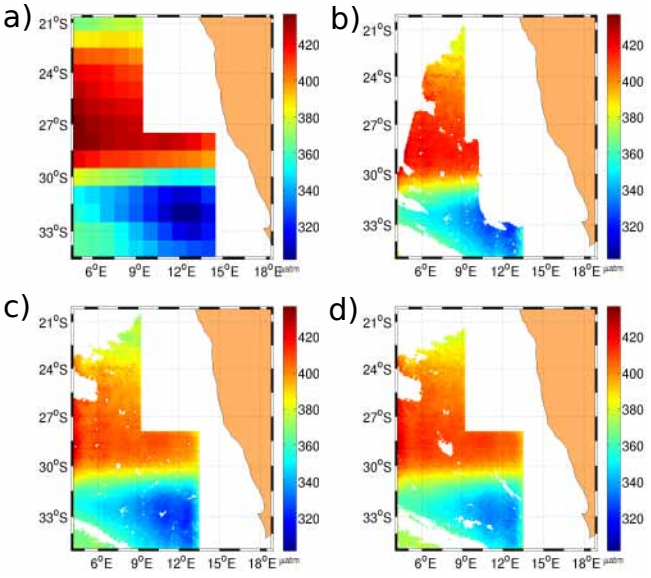

Figure 7. (a) Map of pCO_2 field at low resolution from CarbonTracker. Reconstructed pCO_2 field at super resolution using **(b)** OSTIA SST and MERIS Chl *a*, **(c)** OSTIA SST and GSM-GLOBCOLOUR Chl *a* and **(d)** MODIS SST and GSM-GLOBCOLOUR Chl *a*. All maps correspond to 21 September 2006.

from 5.5–10.5° E, showing that the method not only introduces small-scale features but also modifies the large-scale spatial variability.

5.2 Evaluation of using different satellite products

Since the underlying aim of this work is to develop a methodology to infer super-resolution pCO_2 from space using remote observations, we perform a validation study of the different data used in the inferring computations. This provides us an evaluation where satellite products are more suitable for our methodology and thus gives confidence to our method as well as a better understanding of its limitations. The evaluation analysis is addressed taking into account two main concerns: one related to the number of valid points yielded in the pCO_2^{infer} field, and another with regard to the degradation of the information contained in the transition fronts. A valid point is a pixel where we have simultaneous Chl *a*, SST and pCO_2 values from CarbonTracker, from which we can obtain a value of pCO_2^{infer}, in other words without missing information. One example comparing the reconstructed pCO_2 field obtained from the above-mentioned product combinations is plotted in Fig. 7. The general pattern is quite similar in all of them with some differences in the details of the small scales and in the missing points due to cloudiness (white patches). This example clearly shows how different coverage of the pCO_2 can be in the field depending on the product combination.

Similar results are found when one compares the spatial distribution of the pCO_2^{infer} values to the time averages over 2006 and 2008 for the three product combinations (Fig. 8). The same pattern with an area of higher pCO_2 between 24 and 30° S and lower pCO_2 values outside this region is produced with the three combinations. The most noticeable differences are located in the most northern region and in the southeastern region off Benguela. This can be quantified by computing the standard deviation of the reconstructed pCO_2 values among the different combination of data sets. Figure 8d shows the spatial distribution of the time average over 2006 and 2008 of the standard deviation computed in each pixel among the pCO_2^{infer} values obtained from the three product combinations. The larger values of the dispersion (not greater than 5 µatm) are found in the area between the latitudes of 20° S and 23° S – and in the southern region, in particular, between the latitudes of 31.5° S and 35.5° S – and between the longitudes of 11° E and 13.5° E. The low value of the dispersion indicates that the method is robust when different data sets are used in the inference.

First, we compute the number of valid points in the pCO_2^{infer} field for each product combination. Table 3 summarizes the total number of valid points for each product combination for both years 2006 and 2008. As expected, the number of valid points is found to be the highest for the combina-

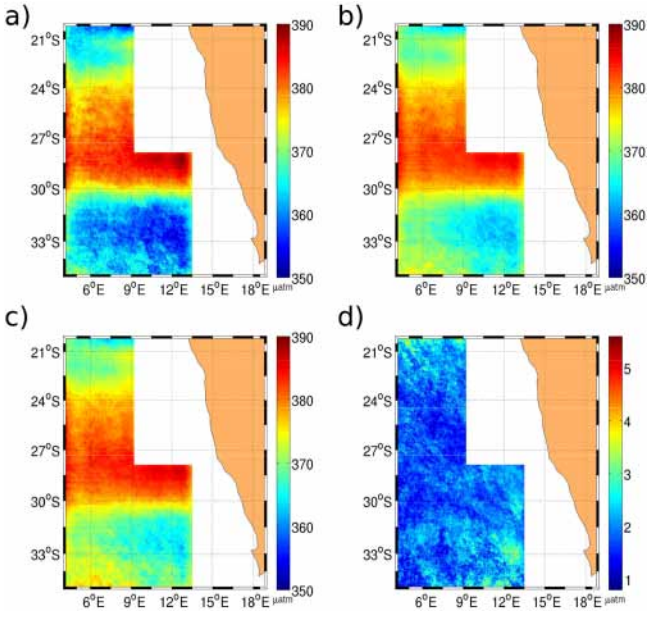

Figure 8. Spatial distribution of the time averages of pCO_2^{infer} values over the years 2006 and 2008 using **(a)** OSTIA SST and MERIS Chl *a*, **(b)** OSTIA SST and GSM-GLOBCOLOUR Chl *a* and **(c)** MODIS SST and GSM-GLOBCOLOUR Chl *a*. **(d)** Map with spatial distribution of the standard deviation for the pCO_2^{infer} among the different combination of the data sets.

Table 3. Number of valid points in the pCO_2 fields and their difference between the three combinations of MERIS or GLOBCOLOUR Chl with OSTIA or MODIS SST in the area of Benguela.

Valid points in the inferred pCO_2 fields: 2006/2008	
No. total pixels domain	55 711 378
No. points OSTIA-MERIS	9800 776
No. points OSTIA-GLOBCOLOUR(AVW)	26 382 072
No. points OSTIA-GLOBCOLOUR(GSM)	27 313 043
No. points MODIS-GLOBCOLOUR(GSM)	20 397 047
OSTIA-GSM/OSTIA-MERIS ratio	2.78
OSTIA-GSM/MODIS-GSM ratio	1.33
MODIS-GSM-/OSTIA-MERIS ratio	1.08
LP_{OM}	82 %
LP_{OG}(AVW)	53 %
LP_{OG}(GSM)	51 %
LP_{MG}	63 %

tion of merged products OSTIA SST and GLOBCOLOUR-GSM, with $N_{GO} = 27\,313\,043$ points, followed by the combination MODIS SST and GLOBCOLOUR Chl with $N_{MG} = 20\,397\,047$ points and finally by the OSTIA SST and MERIS Chl combination with $N_{OM} = 98\,00\,776$ points. Looking at the different proportions, we find that the number of valid points is 2.78 times larger when using the merged products OSTIA and GLOBCOLOUR-GSM than using OSTIA and MERIS, 1.33 times larger than using MODIS and GLOBCOLOUR-GSM and 1.08 times larger using OSTIA SST and GSM Chl *a* than using MODIS SST and GSM Chl *a*. Furthermore, if we know that the total number of pixels in the domain taking out the points of the CarbonTracker mask and for the 2 years is $N_p = 55\,711\,378$, one can estimate the loss of valid points for each combination, LP_x. LP_x is computed by taking the relative difference between the number of total available pixels in the domain N_p and the number of points in the inferred pCO_2 field obtained for each product combination, N_x, and dividing it by the total number of pixels N_p, $LP_x = \frac{N_p - N_x}{N_p} 100\,\%$. Here the subscript x refers to the product combination (e.g., $LP_x = LP_{OM}$, LP_{OG} and LP_{MG} for the loss of valid points with the OSTIA-MERIS, OSTIA-GLOBCOLOUR and MODIS-GLOBCOLOUR product combinations, respectively). The loss of valid points due to cloudiness in the ocean color and SST images is less severe for the OSTIA-GLOBCOLOUR combination, with a loss of 51 %, and is more affected by the cloudiness the OSTIA-MERIS combination with a loss of 82 %.

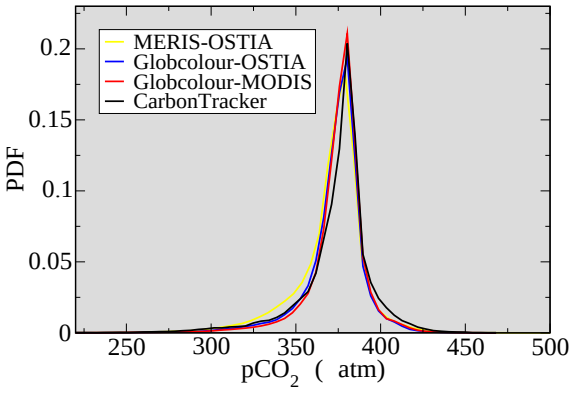

Figure 9. Comparison of the probability distribution functions of CarbonTracker and inferred pCO_2 values over the Benguela area for the three different SST and OC product combinations: MERIS Chl and OSTIA SST, GLOBCOLOUR merged Chl and OSTIA SST, and GLOBCOLOUR merged Chl and MODIS SST.

Next we explore the quality of the information contained in the transition fronts, in particular, in the non-merged products such as MERIS OC and MODIS SST as compared to the merged products: GLOBCOLOUR OC and OSTIA SST. The PDFs of pCO_2 values from CarbonTracker and pCO_2^{infer} values for the three combinations of OC and SST products, i.e., MERIS-OSTIA, GLOBCOLOUR-OSTIA, MODIS-GLOBCOLOUR (see Fig. 9) show that there is a good correspondence of all pCO_2^{infer} values with those from pCO_2^{Ctrack}. Indeed the histograms show also a better agreement between merged products and CarbonTracker: the peak of the PDF for pCO_2^{infer} is closer to the CarbonTracker peak in the case of OSTIA and GLOBCOLOUR than when using MERIS and MODIS products.

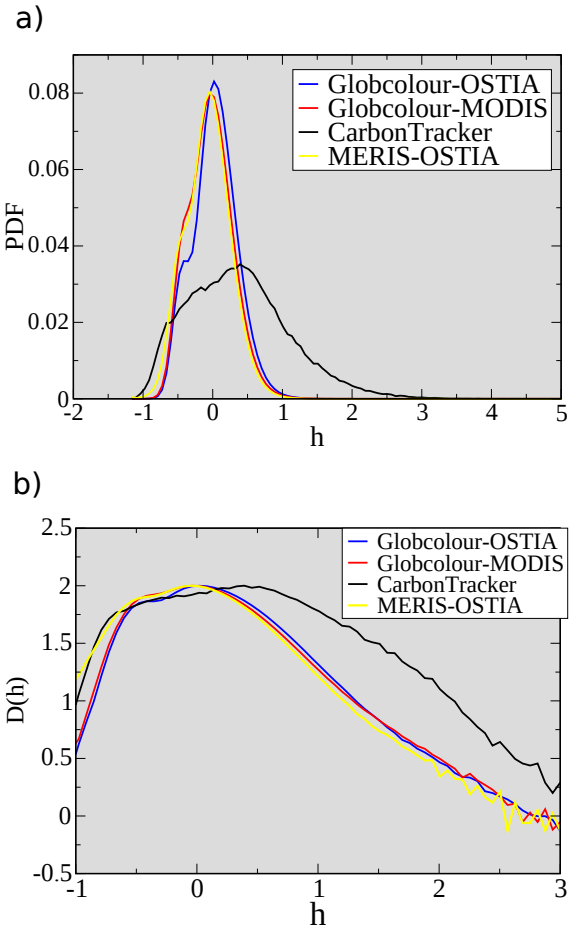

Figure 10. (a) Empirical PDFs for the singularity exponents of pCO_2 fields from CarbonTracker and from the cascade of the three product combinations. **(b)** Associated singularity spectra. In these computations we use all the pCO_2 values obtained in 2006 and 2008.

Furthermore, to examine the transition fronts for the different products, we compute the singularity spectra for the three product combinations (see Fig. 10). At low values of h (singularity exponent), related to the most singular manifolds, the shape of singularity spectrum for inferred data from merged products better matches a binomial cascade, with an improved description of the dimension of the sharpest transition fronts. We know from the theory that tracers advected by the flow in the turbulent regime, as happens in the ocean, shows multifractal behavior with a characteristic singularity spectrum $D(h)$, which is similar, for some types of turbulence, to $D(h)$ for the binomial multiplicative process.

5.3 Validation with in situ measurements

Next, we perform a validation analysis of the results of our super-resolution pCO_2 algorithm with field observations of oceanic pCO_2. We perform the validation using pCO_2 ocean data from in situ measurements (pCO_2^{insitu}) taken in

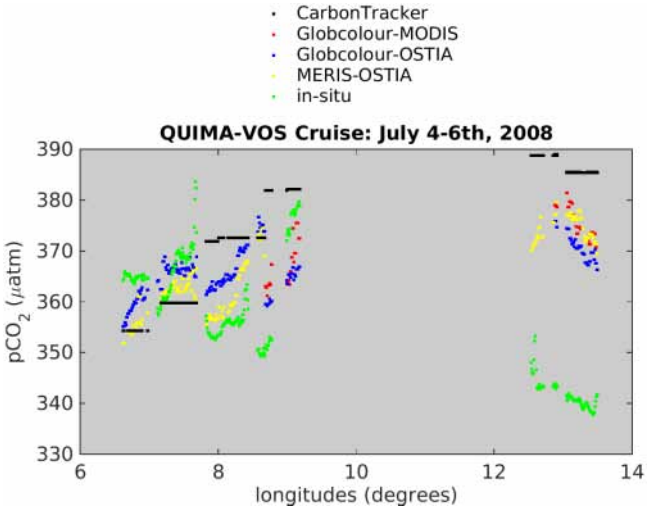

Figure 11. Values of pCO_2^{Ctrack} (black points), pCO_2^{infer} (MODIS-SST/GLOBCOLOUR Chl) (red points), pCO_2^{infer} (OSTIA-SST/GLOBCOLOUR Chl) (blue points) pCO_2^{infer} (OSTIA-SST/MERIS Chl) (yellow points) and pCO_2^{insitu} (green points) as a function of latitude corresponding to the valid intersections during the QUIMA cruise through 4–6 July 2008.

the Benguela region (see Sect. 2.3). We decided to carry out the validation directly on pCO_2 rather than on the air–sea CO_2 flux since the field measurements provide oceanic pCO_2 data.

An example of the qualitative comparison of values of pCO_2^{Ctrack}, pCO_2^{infer} for all the product combinations and pCO_2^{insitu} at the intersections of the QUIMA cruise during 4–7 July 2008, as a function of the longitudinal coordinate of the intersections, is shown in Fig. 11. While there are visible differences between various pCO_2 values, the values of pCO_2^{infer} approximate better pCO_2^{insitu} values than those of pCO_2^{Ctrack}. The small-scale patterns are well reproduced in the inferred pCO_2 field. Values of pCO_2^{infer} exhibit gradients and small-scale fluctuations, likely induced by the presence of fronts, which can be also detected in the profile of the in situ measurements of pCO_2. Most days pCO_2^{infer} and pCO_2^{Ctrack} values overestimate pCO_2^{insitu} values. On some days, pCO_2^{infer} values follow the same trend, with the same small-scale fluctuations as pCO_2^{insitu}.

First, we analyze the number of valid intersections for each product combination. A valid intersection is a placement in space and time common to the inferred, CarbonTracker and in situ pCO_2, without missing values. Among the 20 available cruises in the Benguela during 2005, 2006 and 2008, we find that the total number of in situ measurements in the Benguela region under study is $N_{insitu} = 17\,355$ and within the CarbonTracker domain this number is reduced to $N_{Ctrack} = 8377$ measurements. To estimate the loss of valid intersections due to the land mask of the CarbonTracker, we

Table 4. Mean difference, absolute error and relative error of pCO_2 values obtained from CarbonTracker and pCO_2 values inferred at super resolution with respect to values of pCO_2 measurements during the QUIMA2005/QUIMA2006/QUIMA2008 cruises in the Benguela region.

	OST-MER	OST-GLOB	MOD-GLOB
No. valid intersections	747	1928	1460
L_{infer} (%)	91	76	82
$\text{MD}_{\text{Ctrack}}$ (µatm)	2.97	8.83	14.93
MD_{infer} (µatm)	0.15	3.42	8.42
$\text{AE}_{\text{Ctrack}}$ (µatm)	21.34	22.08	22.07
AE_{infer} (µatm)	17.77	16.47	16.62
$\text{RE}_{\text{Ctrack}}$	0.059	0.060	0.061
RE_{infer}	0.048	0.045	0.046

compute the relative difference of the number of intersections between the cruise trajectories and the CarbonTracker domain with respect to the number of the in situ measurements, $L_{\text{Crack}} = \frac{N_{\text{insitu}} - N_{\text{Ctrack}}}{N_{\text{insitu}}} 100\,\% = 52\,\%$, showing that half of the measurements fall within the coastal region of the Benguela (land masked by CarbonTracker).

The number of valid intersections is the largest with the OSTIA-GLOBCOLOUR combination (Table 4). To quantify the loss of valid intersections between the in situ measurements and points in the pCO_2^{infer} field, likely due to cloudiness, we compute the relative difference between the number of measurements in the CarbonTracker domain and the valid points in the inferred pCO_2 field with respect to the number of intersections measurements of each cruise and the pCO_2^{Ctrack} field, $L_{\text{infer}} = \frac{N_{\text{Ctrack}} - N_{\text{infer}}}{N_{\text{Ctrack}}} 100\,\%$. We repeat such a computation for the three product combinations. The percentage of losses of intersections in inferred field L_{infer} becomes twice as large than in the case of the OSTIA-SST and MERIS Chl combination, and even higher than with the CarbonTracker domain mask.

In order to quantitatively study the difference between pCO_2^{Ctrack} and pCO_2^{insitu} values as well as the difference between pCO_2^{infer} and pCO_2^{insitu} measurements, we compute the following statistical quantities:

– *Mean difference (MD)*: average of all the intersections of the difference between pCO_2^{Ctrack} and pCO_2^{insitu} values as well as the difference between pCO_2^{infer} and pCO_2^{insitu} values at the same intersection, i,

$$\text{MD}_{\text{Ctrack}} = \frac{1}{N}\sum_{i=1}^{N}(pCO_2{}^{\text{Ctrack}}(i) - pCO_2{}^{\text{insitu}}(i)), \quad (5)$$

$$\text{MD}_{\text{infer}} = \frac{1}{N}\sum_{i=1}^{N}(pCO_2{}^{\text{infer}}(i) - pCO_2{}^{\text{insitu}}(i)), \quad (6)$$

where N is the number of intersections.

– *Mean absolute error (AE)*: average of all the intersections of the absolute values of the difference between pCO_2^{Ctrack} or pCO_2^{infer} and pCO_2^{insitu} at the same intersection,

$$\text{AE}_{\text{Ctrack}} = \frac{1}{N}\sum_{i=1}^{N}\left|pCO_2{}^{\text{Ctrack}}(i) - pCO_2{}^{\text{insitu}}(i)\right|, \quad (7)$$

$$\text{AE}_{\text{infer}} = \frac{1}{N}\sum_{i=1}^{N}\left|pCO_2{}^{\text{infer}}(i) - pCO_2{}^{\text{insitu}}(i)\right|. \quad (8)$$

– *Mean relative error (RE)*: average of all the intersections of the errors of the estimated values of pCO_2 (CarbonTracker or inferred) with respect to the reference pCO_2 values (in situ) at the same intersection,

$$\text{RE}_{\text{Ctrack}} = \frac{1}{N}\sum_{i=1}^{N}\left|\frac{pCO_2{}^{\text{Ctrack}}(i) - pCO_2{}^{\text{insitu}}(i)}{pCO_2{}^{\text{insitu}}(i)}\right|, \quad (9)$$

$$\text{RE}_{\text{infer}} = \frac{1}{N}\sum_{i=1}^{N}\left|\frac{pCO_2{}^{\text{infer}}(i) - pCO_2{}^{\text{insitu}}(i)}{pCO_2{}^{\text{insitu}}(i)}\right|. \quad (10)$$

We started the statistical validation by analyzing each QUIMA cruise separately (not shown) and we found that in most of the cruises, the absolute error for inferred pCO_2 is relatively small (less than 15 µatm) except on 21 August 2006 and 17 May 2008, with an error of 44 and 30 µatm, respectively. Then we address the global validation using all available cruises during these years.

We summarize in Table 4 the results of the computations of the errors given by Eq. (7–10) by taking averages of all valid intersections found during 2005, 2006 and 2008. The absolute error, AE is smaller in the three cases of pCO_2^{infer} (17.77, 16.47 and 16.62 µatm for OSTIA-MERIS, OSTIA-GLOBCOLOUR and MODIS-GLOBCOLOUR combinations, respectively) than for pCO_2^{Ctrack} (21.34, 22.08 and 22.07 µatm, respectively), showing that the estimated pCO_2 field at super resolution using our algorithm is improving the pCO_2 field obtained from CarbonTracker. The smallest AE is for the combination of SST and Chl provided by merged products. The values of pCO_2^{Ctrack} are, on average, larger than pCO_2^{insitu} ($\text{MD}_{\text{Ctrack}} = 2.97$, 8.83 and 14.93 µatm) while the differences between pCO_2^{infer} and pCO_2^{insitu} values compensate each other ($\text{MD}_{\text{infer}} = 0.15$, 3.42 and 8.42 µatm). In all cases the $\text{MD}_{\text{Ctrack}}$ and MD_{infer} are positive, meaning that the pCO_2 values are overestimated. Finally, comparing the relative error of pCO_2^{Ctrack} and pCO_2^{infer} with respect to pCO_2^{insitu}, we found that the relative error is low in all cases, smaller for pCO_2^{infer} than for pCO_2^{Ctrack}.

Finally, if we only compare the statistical errors at the common valid intersections between the pCO_2^{infer} using the three product combinations with pCO_2^{Ctrack} and with the in situ measurements (see Table 5), we obtain 458 mutual intersections. We obtain similar results when taking into account all the intersections. The absolute error is smaller in

Table 5. Mean difference, absolute error and relative error of pCO_2 values obtained from CarbonTracker and pCO_2 values inferred at super resolution with respect to values of pCO_2 measurements during the QUIMA2005/QUIMA2006/QUIMA2008 cruises in the Benguela region at the same intersections.

	OST-MER	OST-GLOB	MOD-GLOB
No. valid intersections	458	458	458
MD_{Ctrack} (µatm)	8.01	8.01	8.01
MD_{infer} (µatm)	4.37	1.62	3.32
AE_{Ctrack} (µatm)	23.23	23.23	23.23
AE_{infer} (µatm)	19.92	16.31	18.85
RE_{Ctrack}	0.065	0.065	0.065
RE_{infer}	0.055	0.045	0.051

the case of pCO_2^{infer} (17.65 µatm) than with pCO_2^{Ctrack} (20.24 µatm), indicating that our algorithm improves the estimation of ocean pCO_2. The smallest AE is again for the combination with merged products. MD is positive showing that most of the time pCO_2^{infer} and pCO_2^{Ctrack} values are overestimated (see Fig. 11). Again the relative error is small, less than 0.06, for all the product combinations.

6 Conclusions

In this work we have presented a method to infer high-resolution CO_2 fluxes by propagating the small-scale information given in satellite images across scales. The method is based on a multi-resolution analysis applied to the critical transitions given by singularity exponent analysis. More specifically, we have reconstructed maps of CO_2 fluxes at high resolution (4 km) in the region offshore Benguela using SST and ocean color data at this resolution, and CarbonTracker CO_2 flux data at low resolution (110 km). The inferred representation of ocean surface pCO_2 improves the description provided by CarbonTracker, enhancing the small-scale variability. Spatial fluctuations observed in latitudinal profiles of in situ pCO_2 have also been obtained in the inferred pCO_2, showing that the inferring algorithm captures the small-scale features of the pCO_2 field. The examination of different combinations of ocean color and sea surface temperature (SST) products reveals that using merged products, i.e., GLOBCOLOUR, increases the quality and the number of valid points in the pCO_2 field. We show that mean absolute errors of the inferred values of pCO_2 with respect to in situ measurements are smaller than for CarbonTracker. The statistical comparison of inferred and CarbonTracker pCO_2 values with in situ data shows the potential of our method as well as the shortcomings of using CarbonTracker data for the estimation of air–sea CO_2 fluxes. These results indicate that the outputs of our algorithm will be only as good as the inputs.

We are aware that further investigations could improve the algorithm. The multiple linear regression coefficients could be derived differentiating the seasons (i.e., coefficients would vary as a function of calendar month) considering the marked seasonal cycle in the Benguela upwelling system. Additionally, future work will focus on the extension of the computations to larger areas in order to infer global high-resolution CO_2 fluxes. This will allow more comprehensive and robust validation from more in situ measurements.

Acknowledgements. This work was supported by the ESA Support To Science Element Grant no. 400014715/11/I-NB OceanFlux-Upwelling Theme. The Surface Ocean CO_2 Atlas (SOCAT) is an international effort, supported by the International Ocean Carbon Coordination Project (IOCCP), the Surface Ocean Lower Atmosphere Study (SOLAS), and the Integrated Marine Biogeochemistry and Ecosystem Research program (IMBER), to deliver a uniformly quality-controlled surface ocean CO_2 database. The many researchers and funding agencies responsible for the collection of data and quality control are thanked for their contributions to SOCAT.

Edited by: B. Currie

References

Abraham, E. and Bowen, M.: Chaotic stirring by a mesoscale surface-ocean flow, Chaos, 12, 373–381, 2002.

Abraham, E., Law, C., Boyd, P., Lavender, S., Maldonado, M., and Bowie, A.: Importance of stirring in the development of an iron-fertilized phytoplankton bloom, Nature, 407, 727–730, 2000.

Arneodo, A., Argoul, F., Bacry, E., Elezgaray, J., and J.F., M.: Ondelettes, multifractales et turbulence, Diderot Editeur, Paris, France, 1995.

Bakker, D. C. E., Pfeil, B., Smith, K., Hankin, S., Olsen, A., Alin, S. R., Cosca, C., Harasawa, S., Kozyr, A., Nojiri, Y., O'Brien, K. M., Schuster, U., Telszewski, M., Tilbrook, B., Wada, C., Akl, J., Barbero, L., Bates, N. R., Boutin, J., Bozec, Y., Cai, W.-J., Castle, R. D., Chavez, F. P., Chen, L., Chierici, M., Currie, K., de Baar, H. J. W., Evans, W., Feely, R. A., Fransson, A., Gao, Z., Hales, B., Hardman-Mountford, N. J., Hoppema, M., Huang, W.-J., Hunt, C. W., Huss, B., Ichikawa, T., Johannessen, T., Jones, E. M., Jones, S. D., Jutterström, S., Kitidis, V., Körtzinger, A., Landschützer, P., Lauvset, S. K., Lefèvre, N., Manke, A. B., Mathis, J. T., Merlivat, L., Metzl, N., Murata, A., Newberger, T., Omar, A. M., Ono, T., Park, G.-H., Paterson, K., Pierrot, D., Ríos, A. F., Sabine, C. L., Saito, S., Salisbury, J., Sarma, V. V. S. S., Schlitzer, R., Sieger, R., Skjelvan, I., Steinhoff, T., Sullivan, K. F., Sun, H., Sutton, A. J., Suzuki, T., Sweeney, C., Takahashi, T., Tjiputra, J., Tsurushima, N., van Heuven, S. M. A. C., Vandemark, D., Vlahos, P., Wallace, D. W. R., Wanninkhof, R., and Watson, A. J.: An update to the Surface Ocean CO_2 Atlas (SOCAT version 2), Earth Syst. Sci. Data, 6, 69–90, doi:10.5194/essd-6-69-2014, 2014.

Berti, S. and Lapeyre, G.: Lagrangian reconstructions of temperature and velocity in a model of surface ocean turbulence, Ocean Modell., 76, 59–71, 2014.

Bouchet, F. and Venaille, A.: Statistical mechanics of two-dimensional and geophysical flows, Physics Reports, 515, 227–295, 2012.

Delcroix, T., Alory, G., Cravatte, S., Correge, T., and McPhaden, M.: A gridded sea surface salinity dataset for the tropical Pacific with sample applications (1950–2008), Deep-Sea Res. Pt. I, 58, 38–48, 2011.

Dickey, T.: Emerging ocean observations for interdisciplinary data assimilation systems, J. Marine Syst., 40/41, 5–48, 2003.

Dickson, A. G., Sabine, C. L., and Christian, J. R.: Guide to best practices for ocean CO_2 measurements, PICES Special Publication, 3, 191 pp., 2007.

Donlon, C. J., Martin, M., Stark, J., Roberts-Jones, J., Fiedler, E., and Wimmer, W.: The Operational Sea Surface Temperature and Sea Ice Analysis (OSTIA) system, Remote Sens. Environ., 116, 140–158, 2012.

Franco, A. C., Hernández-Ayón, J. M., Beier, E., Garçon, V., Maske, H., Paulmier, A., Färber-Lorda, J., Castro, R., and Sosa-Ávalos, R.: Air-sea CO_2 fluxes above the stratified oxygen minimum zone in the coastal region off Mexico, J. Geophys. Res. Oceans, 119, 2923–2937, 2014.

Frisch, U.: Turbulence: The Legacy of A.N. Kolgomorov, Cambrige University Press, 1995.

Garbe, C. and Vihharev, J.: Modeling of atmospheric transport of chemical species in the Polar regions, in: IEEE International Geoscience and Remote Sensing Symposium, IEEE, Munich, Germany, 6047–6050, 22–27 July, 2012.

Garbe, C., Handler, R. A., and Jahne, B.: Transport at the Air–Sea Interface – Measurements, Models and Parameterizations, Springer-Verlag, Berlin, ISBN: 978-3-540-36904-2, 2007.

Garbe, C., Rutgersson, A., Boutin, J., Delille, B., Fairall, C., Gruber, N., Hare, J., Ho, D., Johnson, M., de Leeuw, G., Nightingale, P., Pettersson, H., Piskozub, J., Sahlee, E., Tsai, W., Ward, B., Woolf, D., and Zappa, C.: Transfer across the air–sea interface, in: Ocean–Atmosphere Interactions of Gases and Particles, edited by: Liss, P. and Johnson, M., Springer-Verlag, Norwich, UK, 55–112, 2014.

GLOBALVIEW: Cooperative Global Atmospheric Data Integration Project, updated annually. Multi-laboratory compilation of synchronized and gap-filled atmospheric carbon dioxide records for the period 1979–2012. Compiled by NOAA Global Monitoring Division: Boulder, Colorado, USA Data product available at: http://dx.doi.org/10.3334/OBSPACK/1002, 2013.

González-Dávila, M., Santana-Casano, J., and Ucha, I.: Seasonal variability of fCO_2 in the Angola-Benguela region, Prog. Oceanogr., 83, 124–133, 2009.

Gruber, N., Gloor, M., Fletcher, S., Doney, S., Dutkiewicz, S., and co authors: Oceanic sources, sinks and transport of atmospheric CO_2, Global Biogeochem. Cy., 23, GB1005, doi:10.1029/2008GB003349, 2009.

Gutknecht, E., Dadou, I., Le Vu, B., Cambon, G., Sudre, J., Garçon, V., Machu, E., Rixen, T., Kock, A., Flohr, A., Paulmier, A., and Lavik, G.: Coupled physical/biogeochemical modeling including O_2-dependent processes in the Eastern Boundary Upwelling Systems: application in the Benguela, Biogeosciences, 10, 3559–3591, doi:10.5194/bg-10-3559-2013, 2013.

Hales, B., Takahashi, T., and Bandstra, L.: Atmospheric CO_2 uptake by a coastal upwelling system, Global Biogeochem. Cy., 19, GB1009, doi:10.1029/2004GB002295, 2005.

IOCCP: Surface Ocean CO_2 Variability and Vulnerabilities Workshop, Rep. 7, U.N. Educ., Sci. and Cult. Organ., Paris, 5, 2007.

Klein, P. and Lapeyre, G.: The oceanic Vertical Pump Induced by Mesoscale and Submesoscale Turbulence, Annu. Rev. Mar. Sci., 1, 351–75, 2009.

Landschützer, P., Gruber, N., Bakker, D., and Schuster, U.: Recent variability of the global ocean carbon sink, Global Biogeochem. Cy., 28, 927–949, 2014.

Mahadevan, A., Lévy, M., and Mémery, L.: Mesoscale variability of sea surface pCO_2: What does it respond to?, Global Biogeochem. Cy., 18, GB1017, doi:10.1029/2003GB002102, 2004.

Maji, S. K. and Yahia, H. M.: Edges, transitions and criticality, Pattern Recognition, 47, 2104–2115, 2014.

Maritorena, S. and Siegel, D. A.: Consistent merging of satellite ocean color data sets using a bio-optical model, Remote Sens. Environ., 94, 429–440, 2005.

Monteiro, P.: Eastern boundary currents: The Benguela Current System, in: Carbon and Nutrient Fluxes in: Continental Margins: A Global Synthesis, Chap. 2, edited by: Liu, K., Atkinson, L., Quiñones, R., and Talaue-McManus, L., Springer, Berlin, 65–78, 2010.

Montes, I., Dewitte, B., Gutknecht, E., Paulmier, A., Dadou, I., Oschlies, A., and Garçon, V.: High-resolution modeling of the Eastern Tropical Pacific Oxygen Minimum Zone: Sensitivity to the tropical oceanic circulation, J. Geophys. Res.-Oceans, 119, 5515–5532, 2014.

Paulmier, A., Ruiz-Pino, D., and Garçon, V.: The Oxygen Minimum Zone (OMZ) off Chile as intense source of CO_2 and N_2O, Contin. Shelf Res., 28, 2746–2756, 2008.

Paulmier, A., Ruiz-Pino, D., and Garçon, V.: CO_2 maximum in the oxygen minimum zone (OMZ), Biogeosciences, 8, 239–252, doi:10.5194/bg-8-239-2011, 2011.

Peters, W., Jacobson, A., C. Sweeney, A. A., Conway, T., Masarie, K., J.B. Miller, a. L. B., Petron, G., Hirsch, A., Worthy, D., van der Werf, G., Randerson, J., Wennberg, P., Krol, M., and Tans, P.: An atmospheric perspective on North American carbon dioxide exchange : CarbonTracker, Proc. Natl. Acad. Sci. USA, 104, 18925–18930, 2007.

Pfeil, B., Olsen, A., Bakker, D. C. E., Hankin, S., Koyuk, H., Kozyr, A., Malczyk, J., Manke, A., Metzl, N., Sabine, C. L., Akl, J., Alin, S. R., Bates, N., Bellerby, R. G. J., Borges, A., Boutin, J., Brown, P. J., Cai, W.-J., Chavez, F. P., Chen, A., Cosca, C., Fassbender, A. J., Feely, R. A., González-Dávila, M., Goyet, C., Hales, B., Hardman-Mountford, N., Heinze, C., Hood, M., Hoppema, M., Hunt, C. W., Hydes, D., Ishii, M., Johannessen, T., Jones, S. D., Key, R. M., Körtzinger, A., Landschützer, P., Lauvset, S. K., Lefèvre, N., Lenton, A., Lourantou, A., Merlivat, L., Midorikawa, T., Mintrop, L., Miyazaki, C., Murata, A., Nakadate, A., Nakano, Y., Nakaoka, S., Nojiri, Y., Omar, A. M., Padin, X. A., Park, G.-H., Paterson, K., Perez, F. F., Pierrot, D., Poisson, A., Ríos, A. F., Santana-Casiano, J. M., Salisbury, J., Sarma, V. V. S. S., Schlitzer, R., Schneider, B., Schuster, U., Sieger, R., Skjelvan, I., Steinhoff, T., Suzuki, T., Takahashi, T., Tedesco, K., Telszewski, M., Thomas, H., Tilbrook, B., Tjiputra, J., Vandemark, D., Veness, T., Wanninkhof, R., Watson, A. J., Weiss, R., Wong, C. S., and Yoshikawa-Inoue, H.: A uniform, quality controlled Surface Ocean CO_2 Atlas (SOCAT), Earth Syst. Sci. Data, 5, 125–143, doi:10.5194/essd-5-125-2013, 2013.

Pont, O., Turiel, A., and J., P.-V. C.: On optimal wavelet bases for the realization of microcanonical cascade processes, Int. J. Wavelets Multiresolut Inf. Process., 9, 35–61, 2011a.

Pont, O., Turiel, A., and Yahia, H.: An optimized algorithm for the evaluation of local singularity exponents in digital signals., vol. LNCS 6636 of 14th International Workshop on Combinatorial Image Analysis (IWCIA 2011), Springer-Verlag, Madrid, 2011b.

Pottier, C., Turiel, A., and Garçon, V.: Inferring mising data in satellite chlorophyll maps using turbulent cascading, Remote Sens. Environ., 112, 4242–4260, 2008.

Rind, D.: Complexity and climate, Science, 284, 105–107, 1999.

Rödenbeck, C., Bakker, D. C. E., Metzl, N., Olsen, A., Sabine, C., Cassar, N., Reum, F., Keeling, R. F., and Heimann, M.: Interannual sea–air CO_2 flux variability from an observation-driven ocean mixed-layer scheme, Biogeosciences, 11, 4599–4613, doi:10.5194/bg-11-4599-2014, 2014.

Sabine, C. L., Hankin, S., Koyuk, H., Bakker, D. C. E., Pfeil, B., Olsen, A., Metzl, N., Kozyr, A., Fassbender, A., Manke, A., Malczyk, J., Akl, J., Alin, S. R., Bellerby, R. G. J., Borges, A., Boutin, J., Brown, P. J., Cai, W.-J., Chavez, F. P., Chen, A., Cosca, C., Feely, R. A., González-Dávila, M., Goyet, C., Hardman-Mountford, N., Heinze, C., Hoppema, M., Hunt, C. W., Hydes, D., Ishii, M., Johannessen, T., Key, R. M., Körtzinger, A., Landschützer, P., Lauvset, S. K., Lefèvre, N., Lenton, A., Lourantou, A., Merlivat, L., Midorikawa, T., Mintrop, L., Miyazaki, C., Murata, A., Nakadate, A., Nakano, Y., Nakaoka, S., Nojiri, Y., Omar, A. M., Padin, X. A., Park, G.-H., Paterson, K., Perez, F. F., Pierrot, D., Poisson, A., Ríos, A. F., Salisbury, J., Santana-Casiano, J. M., Sarma, V. V. S. S., Schlitzer, R., Schneider, B., Schuster, U., Sieger, R., Skjelvan, I., Steinhoff, T., Suzuki, T., Takahashi, T., Tedesco, K., Telszewski, M., Thomas, H., Tilbrook, B., Vandemark, D., Veness, T., Watson, A. J., Weiss, R., Wong, C. S., and Yoshikawa-Inoue, H.: Surface Ocean CO_2 Atlas (SOCAT) gridded data products, Earth Syst. Sci. Data, 5, 145–153, doi:10.5194/essd-5-145-2013, 2013.

Santana-Casiano, J., González-Dávila, M., and Ucha, I.: Carbon dioxide fluxes in the Benguela upwelling system during winter and spring: A comparison between 2005 and 2006, Deep-Sea Res. Pt. II, 56, 533–541, 2009.

Savtchenko, A., Ouzounov, D., Ahmad, S., Acker, J., Leptoukh, G., Koziana, J., and Nickless, D.: Terra and Aqua MODIS products available from NASA GES DAAC, Adv. Space Res., 34, 710–714, 2004.

Sudre, J., Yahia, H., Pont, O., and Garçon, V.: Ocean turbulent dynamics at super resolution from optimal multiresolution analysis and multiplicative cascade, IEEE Trans. Geosci. Remote Sens., 53, 6274–6285, 2015.

Sweeney, C., Gloor, E., Jacobson, A., Key, R., McKinley, G., Sarmiento, J., and Wanninkhof, R.: Constraining global air-sea gas exchange for CO_2 with recent bomb 14C measurements, Global Biogeochem. Cy., 21, GB2015, doi:10.1029/2006GB002784, 2007.

Takahashi, T., Sutherland, S. C., Sweeney, C., Poisson, A., Metzl, N., Tilbrook, B., Bates, N., Wanninkhof, R., Feely, R., Sabine, C., Olafsson, J., and Nojiri, Y.: Global sea-air CO_2 flux based on climatological surface ocean pCO_2, and seasonal biological and temperature effects, Deep-Sea Res. Pt. II, 49, 1601–1622, 2002.

Takahashi, T., Sutherland, S. C., Sweeney, C., Feely, R. A., Chipman, D. W., Hales, B., Friederich, G., Chavez, F., Sabine, C., Watson, A., Bakker, D. C. E., Schuster, U., Metzl, N., Yoshikawa-Inoue, H., Ishii, M., Midorikawa, T., Nojiri, Y., Kortzinger, A., Steinhoff, T., Hoppema, M., Olaffson, J., Anarson, T. S., Tilbrook, B., Johannessen, T., Olsen, A., Bellerby, R., Wong, C. S., Delille, B., Bates, N. R., and de Baar, H. J. W.: Climatological mean and decadal change in surface ocean pCO_2, and net sea-air CO_2 flux over the global oceans, Deep-Sea Res. Pt. II, 56, 554–577, 2009.

Telszewski, M., Chazottes, A., Schuster, U., Watson, A. J., Moulin, C., Bakker, D. C. E., González-Dávila, M., Johannessen, T., Körtzinger, A., Lüger, H., Olsen, A., Omar, A., Padin, X. A., Ríos, A. F., Steinhoff, T., Santana-Casiano, M., Wallace, D. W. R., and Wanninkhof, R.: Estimating the monthly pCO_2 distribution in the North Atlantic using a self-organizing neural network, Biogeosciences, 6, 1405–1421, doi:10.5194/bg-6-1405-2009, 2009.

Turiel, A., Isern-Fontanet, J., García-Ladona, E., and Font, J.: Multifractal Method for the Instantaneous Evaluation of the Stream Function in Geophysical Flows, Phys. Rev. Lett., 95, 104502, doi:10.1103/PhysRevLett.95.104502, 2005.

Turiel, A., Yahia, H., and Pérez-Vicente, C.: Microcanonical multifractal formalism-a geometrical approach to multifractal systems: Part I. Singularity analysis., J. Phys. A: Math. Theor., 41, 15501–15536, 2008.

Valsala, V. and Maksyutov, S.: Simulation and assimilation of global ocean pCO_2 and air–sea CO_2 fluxes using ship observations of surface ocean pCO_2 in a simplified biogeochemical offline model, Tellus B, 62, 821–840, 2010.

Waldron, H. N., Monteiro, P. M. S., and Swart, N. C.: Carbon export and sequestration in the southern Benguela upwelling system: lower and upper estimates, Ocean Sci., 5, 711–718, doi:10.5194/os-5-711-2009, 2009.

Weiss, R.: Carbon doxide in water and sewater: the solubility of a non-ideal gas, Mar. Chem., 2, 203–215, 1974.

Yahia, H., Sudre, J., Pottier, C., and Garçon, V.: Motion analysis in oceanographic satellite images using multiscale methods and the energy cascade, Pattern Recognition, 43, 3591–3604, 2010.